

# Evidence for Stepwise Formation of Amyloid Fibrils by the Mouse Prion Protein

Shweta Jain and Jayant B. Udgaonkar\*

National Centre for Biological Sciences, Tata Institute of Fundamental Research, Bangalore 560065, India

Received 16 April 2008;  
received in revised form  
28 June 2008;  
accepted 21 July 2008  
Available online  
26 July 2008

The full-length mouse prion protein, moPrP, is shown to form worm-like amyloid fibrils at pH 2 in the presence of 0.15 M NaCl, in a slow process that is accelerated at higher temperatures. Upon reduction in pH to 2, native moPrP transforms into a mixture of soluble  $\beta$ -rich oligomers and  $\alpha$ -rich monomers, which exist in a slow, concentration-dependent equilibrium with each other. It is shown that only the  $\beta$ -rich oligomers and not the  $\alpha$ -rich monomers, can form worm-like amyloid fibrils. The mechanism of formation of the worm-like amyloid fibrils from the  $\beta$ -rich oligomers has been studied with four different physical probes over a range of temperatures and over a range of protein concentrations. The observed rate of fibrillation is the same, whether measured by changes in ellipticity at 216 nm, in thioflavin fluorescence upon binding, or in the mean hydrodynamic radius. The observed rate is significantly slower when monitored by total scattering intensity, suggesting that lateral association of the worm-like fibrils occurs after they form. The activation energy for worm-like fibril formation was determined to be 129 kJ/mol. The observed rate of fibrillation increases with an increase in protein concentration, but saturates at protein concentrations above 50  $\mu$ M. The dependence of the observed rate of fibrillation on protein concentration suggests that aggregate growth is rate-limiting at low protein concentration and that conformational change, which is independent of protein concentration, becomes rate-limiting at higher protein concentrations. Hence, fibril formation by moPrP occurs in at least two separate steps. Longer but fewer worm-like fibrils are seen to form at low protein concentration, and shorter but more worm-like fibrils are seen to form at higher protein concentrations. This observation suggests that the  $\beta$ -rich oligomers grow progressively in size to form critical higher order-oligomers from which the worm-like amyloid fibrils then form.

© 2008 Elsevier Ltd. All rights reserved.

**Keywords:** protofibrils; worm-like fibrils; amyloid fibrils; mouse prion protein; protein aggregation

Edited by S. Radford

## Introduction

The molecular basis of the prion diseases appears to be the autocatalytic conversion of the cellular form of the prion protein, PrP<sup>C</sup>, to an alternative conformation, PrP<sup>Sc</sup>.<sup>1</sup> The prion diseases, which include transmissible spongiform encephalopathies and neurodegenerative diseases such as kuru, Creutzfeldt–Jakob disease, and fatal familial insomnia in humans, as well

as scrapie and bovine spongiform encephalopathy in animals, are characterized by the formation of ordered prion protein aggregates by PrP<sup>Sc</sup>.<sup>1–7</sup> While PrP<sup>C</sup> is monomeric and sensitive to protease digestion, PrP<sup>Sc</sup> appears to be richer in  $\beta$ -sheet content, has a low solubility, and is resistant to protease digestion.<sup>1–8</sup> The structure and size (aggregation state) of PrP<sup>Sc</sup> are unknown, but it has been implicated as the infectious agent according to the “protein-only” hypothesis for the propagation of prion diseases.<sup>1,8</sup> Hence, it is crucial to understand the mechanism of the conformational changes that the prion protein undergoes when it self-assembles into the ordered protein aggregates characteristic of prion diseases.

PrP<sup>Sc</sup> can convert PrP<sup>C</sup> into its pathogenic PrP<sup>Sc</sup> self.<sup>1,2,4,5</sup> Different models have been proposed to

\*Corresponding author. E-mail address:

[jayant@ncbs.res.in](mailto:jayant@ncbs.res.in).

Abbreviations used: moPrP, mouse prion protein; ThT, thioflavin T; SI, scattering intensity; DLS, dynamic light scattering; AFM, atomic force microscopy.

explain the conversion process, such as heterodimer polymerization,<sup>9</sup> templated assembly,<sup>10</sup> and nucleation-dependent assembly.<sup>11</sup> It is not known how similar the conversion of PrP<sup>C</sup> to PrP<sup>Sc</sup> by PrP<sup>Sc</sup> is to the conversion of a soluble protein into amyloid fibrils by seeds of the fibrils. PrP<sup>Sc</sup> tends to aggregate and form prion rods, which can bind to amyloid-specific dyes and which, like amyloid fibrils, have core structures that are highly resistant to protease cleavage.<sup>1</sup> The conversion of PrP<sup>C</sup> into PrP<sup>Sc</sup> has been shown to be associated with the formation of stable prion protein aggregates.<sup>1-7</sup> These aggregates have been shown to be amyloid-like in their properties,<sup>12-14</sup> and it appears that they are similar to the amyloid fibril aggregates that the prion protein can be induced to form *in vitro*.<sup>5,15-18</sup> The formation of stable aggregates of the prion protein is linked to prion toxicity and infectivity in prion disorders.<sup>1,2,5,19</sup> Amyloid fibrils formed by the same prion protein can show structural polymorphism,<sup>20</sup> which appears to underlie prion strain diversity.<sup>1,3,5,21-24</sup> It is important to determine when and how structural polymorphism develops during the process of amyloid fibril formation by the prion protein.

Soluble oligomers and protofibrils, rather than the mature amyloid fibrils, appear to be the toxic species in amyloid-related disorders.<sup>25-27</sup> By analogy, prion protein oligomers and prefibrillar aggregates might be the toxic entities in prion disorders.<sup>28,29</sup> In fact, soluble oligomers of the prion protein, 17–27 nm in diameter and 300–600 kDa in mass, derived from the disaggregation of PrP<sup>Sc</sup>, have been shown to compose the most infectious species.<sup>30</sup> These oligomers were also shown to be efficient converters of PrP<sup>C</sup> into a protease-resistant form in an *in vitro* assay, more so than larger fibrils.<sup>30</sup> Hence, it becomes necessary to understand the mechanism of formation of prefibrillar aggregates (soluble oligomers and protofibrils) of the prion protein.

Recombinant prion protein retains the disulfide bond between C179 and C214 of the original mammalian protein, but unlike the latter, it is not glycosylated at N181 and N193, nor does it have a GPI anchor at the C-terminus. Nevertheless, it serves as a very useful model for studying the molecular mechanism of the conversion of PrP<sup>C</sup> to PrP<sup>Sc</sup>. In partially denaturing conditions and in the presence of salt, the protein has been shown to oligomerize into  $\beta$ -oligomers, existing in equilibrium with monomeric PrP ( $\alpha$ -PrP).<sup>31-33</sup> The  $\beta$ -oligomers appear to be off-pathway species incapable of forming long straight fibrils. In contrast,  $\alpha$ -PrP appears to form long straight amyloid fibrils.<sup>32-34</sup> In most studies, truncated versions of prion proteins have been used to characterize the process of protein aggregation.<sup>17,31,32,35-40</sup> These truncated versions include PrP 90–231 and PrP 121–231. Hence, the truncated proteins contain the folded C-terminal domain with its three long  $\alpha$ -helices and two short  $\beta$ -strands,<sup>41-43</sup> but the mostly disordered N-terminus with its glycine-rich octapeptide repeats<sup>42,44</sup> is missing. The N-terminal region has, however, been shown to be crucial in modulating prion protein misfolding and

aggregation.<sup>45-47</sup> Moreover, it has been proposed that expansion of the N-terminal octapeptide repeat region plays a role in inheritable prion disorders.<sup>3</sup> Thus, it is important to understand the mechanism of aggregation of the full-length prion protein.

In this report, the aggregation of the full-length mouse prion protein (moPrP) has been studied at low pH in the presence of salt. Under these conditions, the native prion protein transforms into an equilibrium mixture of soluble  $\beta$ -rich oligomers and  $\alpha$ -rich monomers. It is shown that the  $\beta$ -rich oligomers transform into worm-like amyloid fibrils, but not into long straight fibrils, in a slow process that speeds up at higher temperatures. The kinetics of amyloid fibrillation from the  $\beta$ -rich oligomers has been studied using four different probes: thioflavin T (ThT) fluorescence, which reports on conformational conversion; ellipticity at 216 nm ( $\theta_{216}$ ), which also reports on conformational conversion; hydrodynamic radius ( $R_H$ ), which reports on aggregate elongation; and total scattering intensity (SI), which reports on the size and amount of aggregated material. The results suggest that the process of formation of worm-like amyloid fibrils occurs in multiple step and *via* multiple routes. The kinetics of amyloid fibrillation from the  $\beta$ -rich oligomers do not exhibit any lag phase, and the process does not appear to show any of the characteristic features of nucleation-dependent polymerization.

## Results

### Formation of $\beta$ -rich oligomers of the mouse prion protein

At pH 4, the far-UV CD spectrum of moPrP shows minima at 222 and 209 nm, which is characteristic of an  $\alpha$ -helix-rich protein (Fig. 1a). The distribution of  $R_H$  in terms of percent scattering intensity shows a maximum at  $\sim 2.8$  nm, and tails toward higher values of  $R_H$  (Fig. 1b). To correct for the dominance of the larger aggregates, the percent SI distribution was converted into a percent mass distribution (Fig. 1b, inset). The value of the mean  $R_H$ , as obtained from the percent mass distribution, is found to be  $\sim 2.3$  nm, and no evidence for the presence of oligomers is seen (Fig. 1b, inset). This suggests that moPrP is predominantly monomeric at pH 4 and that a negligible amount ( $<1\%$ ) of oligomers is present.

Upon a reduction of the pH to 2 in the presence of 0.15 M NaCl, native moPrP, at a concentration of 25  $\mu$ M, is seen to transform into an alternative conformation, which is predominantly  $\beta$ -rich, as inferred from the minimum at 216 nm in the far-UV CD spectrum (Fig. 1a). This alternative conformation is shown by dynamic light-scattering (DLS) measurements to have a mean  $R_H$  of  $\sim 13$  nm (Fig. 1b). Hence, upon lowering the pH in the presence of salt, the  $\alpha$ -helix-rich monomeric protein is transformed into soluble  $\beta$ -rich oligomers. The size and the  $\beta$ -sheet content of these oligomers were seen not to change upon incubation at 25  $^{\circ}$ C from 0.5 h to up

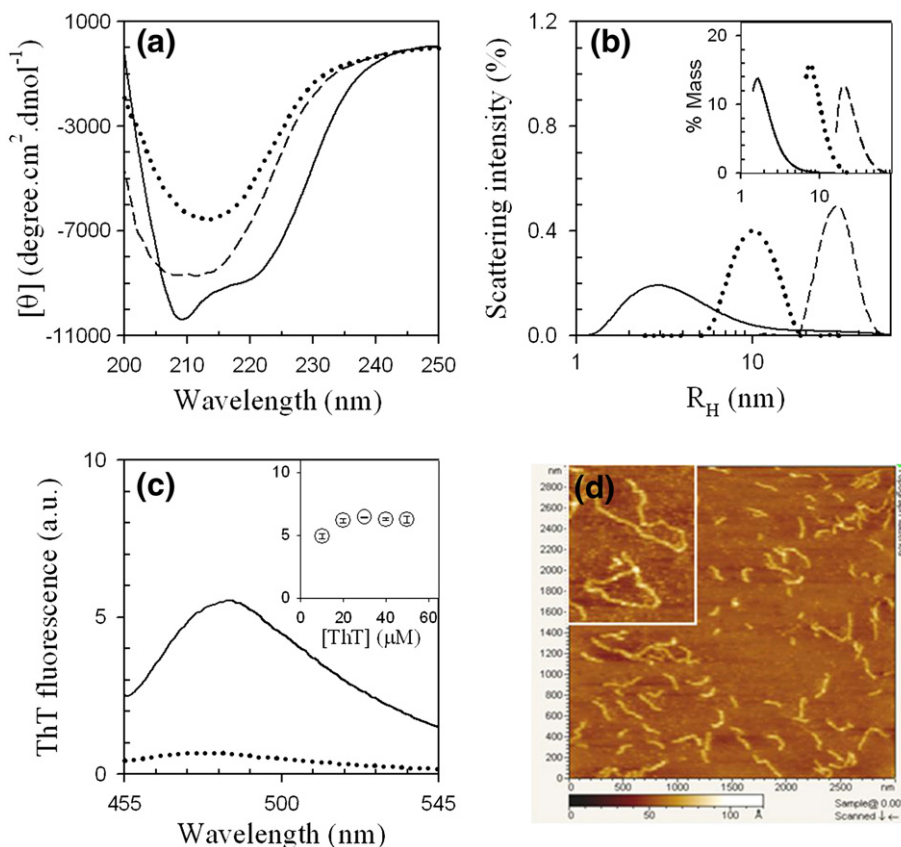


**Fig. 1.** Formation of worm-like amyloid fibrils by 25  $\mu\text{M}$  moPrP, pH 2, at 60  $^{\circ}\text{C}$ . (a) Far-UV CD spectra. (b) Distribution of hydrodynamic radii. The inset shows the distributions of hydrodynamic radii in terms of percent mass. In (a) and (b), the continuous lines, dotted lines, and dashed lines represent the native protein at pH 4; the  $\beta$ -rich oligomer at pH 2, 25  $^{\circ}\text{C}$ , prior to heating; and the fibrils formed at 3 h of heating, respectively. (c) ThT fluorescence spectra of 20  $\mu\text{M}$  ThT with 2  $\mu\text{M}$  protein from an unheated sample corresponding to the  $\beta$ -rich oligomer (dotted line) and 20  $\mu\text{M}$  ThT with 2  $\mu\text{M}$  protein added from a 3-h-heated sample corresponding to worm-like fibrils (continuous line). The inset shows the dependence of the ThT fluorescence signal on the concentration of ThT when protein from a 2-h-heated sample was added at a final concentration of 2  $\mu\text{M}$ . (d) AFM image of worm-like amyloid fibrils formed at 3 h of heating at 60  $^{\circ}\text{C}$ . The inset shows an AFM image of worm-like amyloid fibrils formed when a 3-h-heated sample was incubated at 25  $^{\circ}\text{C}$  for 14 days. The scale bar also applies to the inset.

to 4 h (data not shown). In all the experiments reported here, the  $\beta$ -rich oligomers were incubated for 1 h at pH 2, 25  $^{\circ}\text{C}$ , prior to the temperature jump used to initiate the process of fibrillation.

### Formation of worm-like amyloid fibrils from the $\beta$ -rich oligomers

Upon heating at 60  $^{\circ}\text{C}$ , the  $\beta$ -rich oligomer is transformed into a form that is better able to bind ThT (Fig. 1c) and which manifests itself as elongated, curly worm-like nanostructures in atomic force microscopy (AFM) images (Fig. 1d). Although these resemble in appearance the protofibrils formed by the amyloid- $\beta$  protein,<sup>48,49</sup> it is not known at present whether they, like amyloid- $\beta$  protofibrils, can transform into long straight amyloid fibrils. Upon prolonged incubation, they do become longer but do not straighten out (Fig. 1d, inset). Hence, the elongated nanostructures formed by moPrP are more appropriately called worm-like fibrils, in accordance with the terminology used for similar-looking structures

formed by  $\beta_2$ -microglobulin.<sup>50</sup> The transformation of the  $\beta$ -rich oligomers into worm-like amyloid fibrils is associated with an increase in  $\beta$ -sheet content (Fig. 1a),  $R_H$  (Fig. 1b), and ThT-binding sites (Fig. 1c). The mean  $R_H$  of the worm-like fibrils is found to be 30 nm. In the ThT assay solution, the concentration of the ThT was typically 10-fold in excess of the protein concentration. When the protein concentration was kept fixed at 2  $\mu\text{M}$  and the ThT concentration was varied from 10 to 50  $\mu\text{M}$ , the fluorescence emission at 482 nm did not change (Fig. 1c, inset). This suggests that a 5-fold excess of ThT in the assay solution is sufficient for the measurements. In all the experiments reported here, a 10-fold excess of ThT concentration over the protein concentration was used.

### The $\beta$ -rich oligomers exist in equilibrium with $\alpha$ -rich monomers at pH 2

While Fig. 1 shows that at 25  $\mu\text{M}$  protein concentration, moPrP exists predominantly as a  $\beta$ -rich oligomer at pH 2, it was important to determine

whether the  $\beta$ -rich oligomer exists in equilibrium with any monomeric protein. The far-UV CD spectra of moPrP at different protein concentrations (Fig. 2a) suggest that protein conformation does indeed change with a change in protein concentration. It is seen that at 5  $\mu\text{M}$  protein concentration, an  $\alpha$ -rich form is the predominant form present at pH 2. On the other hand, the spectrum of 25  $\mu\text{M}$  protein indicates that the  $\beta$ -rich form predominates. The spectra were obtained after 1 h of incubation at pH 2; in all cases, identical spectra were obtained after 2 h of incubation.

Figure 2b shows gel-filtration elution profiles of moPrP at different protein concentrations. At 25  $\mu\text{M}$  protein concentration, the predominant (>90%) species elutes out over a range of volume that straddles the void volume and a volume corresponding to the upper limit (300 kDa) of the fractionation range of the column. The gel-filtration data therefore confirm the results of the DLS experiments that show that the predominant species at high protein concentration is a large oligomer (Fig. 1b). At 5  $\mu\text{M}$  protein concentration, the predominant (~75%) species elutes out at the lower limit of the fractionation range of the column, at a volume similar to where native moPrP at pH 4 elutes out. The predominant species at low protein concentration appears, therefore, to be a monomer. The far-UV CD spectra of the protein at concentrations of 5 and 25  $\mu\text{M}$  (Fig. 2a) indicate that the oligomer is  $\beta$ -rich, while the monomer is  $\alpha$ -rich.

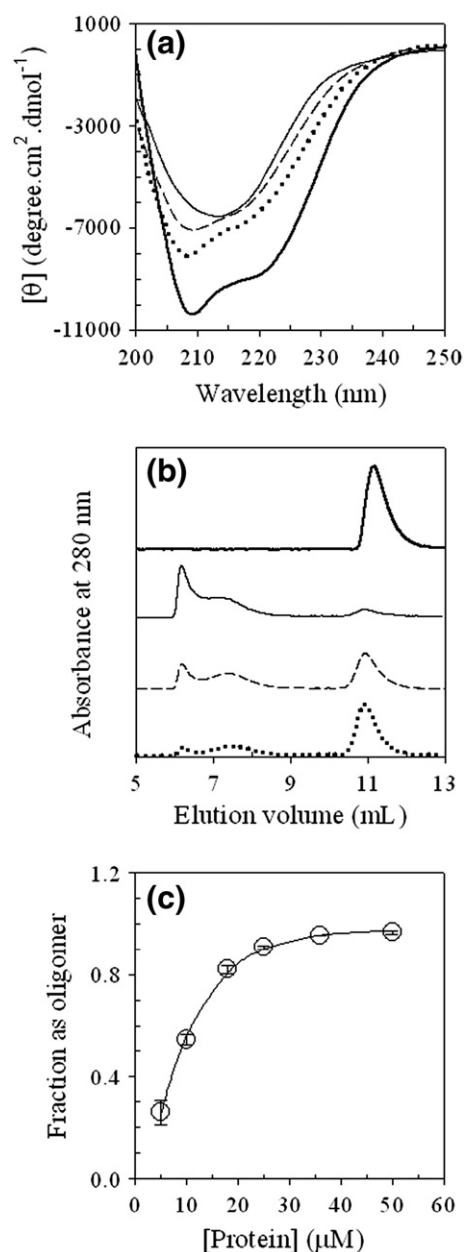
Figure 2c indicates that the fraction of protein present as the  $\beta$ -rich oligomer increases with an increase in total protein concentration (measured as

monomer concentration). At protein concentrations greater than 25  $\mu\text{M}$ , more than 95% of the protein exists as the  $\beta$ -rich oligomer. The observation of both species in the elution profiles obtained from gel filtration at different protein concentrations indicates that the  $\beta$ -rich oligomer and the  $\alpha$ -rich monomer interconvert on a time scale that is slow compared to the time of chromatography (~20 min).

### Kinetics of amyloid fibrillation monitored by multiple probes

Figure 3a and b show the ThT fluorescence- and  $\theta_{216}$ -monitored kinetics, respectively, of amyloid fibrillation at 60  $^{\circ}\text{C}$ , by 25  $\mu\text{M}$  moPrP. In both cases, the kinetics are monophasic with no apparent lag phase. The observed rates of formation of the worm-like amyloid fibrils are similar when moni-

**Fig. 2.** Dependence on protein concentration of the population of the  $\beta$ -rich oligomer at pH 2, 25  $^{\circ}\text{C}$ . (a) Far-UV CD spectra of 25  $\mu\text{M}$  (thin continuous line), 10  $\mu\text{M}$  (dashed line), and 5  $\mu\text{M}$  (dotted line) moPrP. Also shown is the spectrum of 25  $\mu\text{M}$  native moPrP at pH 4 (thick continuous line). (b) The elution profile on a Waters SW-300 size-exclusion column was determined from measurement of the absorbance at 280 nm of the eluant. The  $\beta$ -rich oligomer elutes out between 6 and 8.5 mL, while a monomer elutes out between 10.3 and 12 mL. Elution profiles are shown for 50  $\mu\text{l}$  of 25  $\mu\text{M}$  (thin continuous line), 10  $\mu\text{M}$  (dashed line), and 5  $\mu\text{M}$  (dotted line) protein injected into the column. Also shown is the elution profile observed for 25  $\mu\text{M}$  native moPrP at pH 4 (thick continuous line): native moPrP at pH 4 elutes out 0.25 mL later than does the  $\alpha$ -rich monomer at pH 2. To normalize the elution profiles of 10 and 5  $\mu\text{M}$  samples to those of the 25  $\mu\text{M}$  samples, the absorbance values were multiplied by factors of 2.5 and 5, respectively. (c) Dependence of the fractional population of  $\beta$ -rich oligomer on protein concentration. The fraction of protein present as  $\beta$ -rich oligomer was determined by dividing the area under the  $\beta$ -rich oligomer eluant peak obtained upon gel filtration by the total area under both the  $\beta$ -rich oligomer and monomer peaks, when elution was monitored by measurement of absorbance at 280 nm. The protein concentration refers to the total monomer concentration. The error bars represent the spread in the data from two separate experiments, and the continuous line through the data was drawn by inspection only.



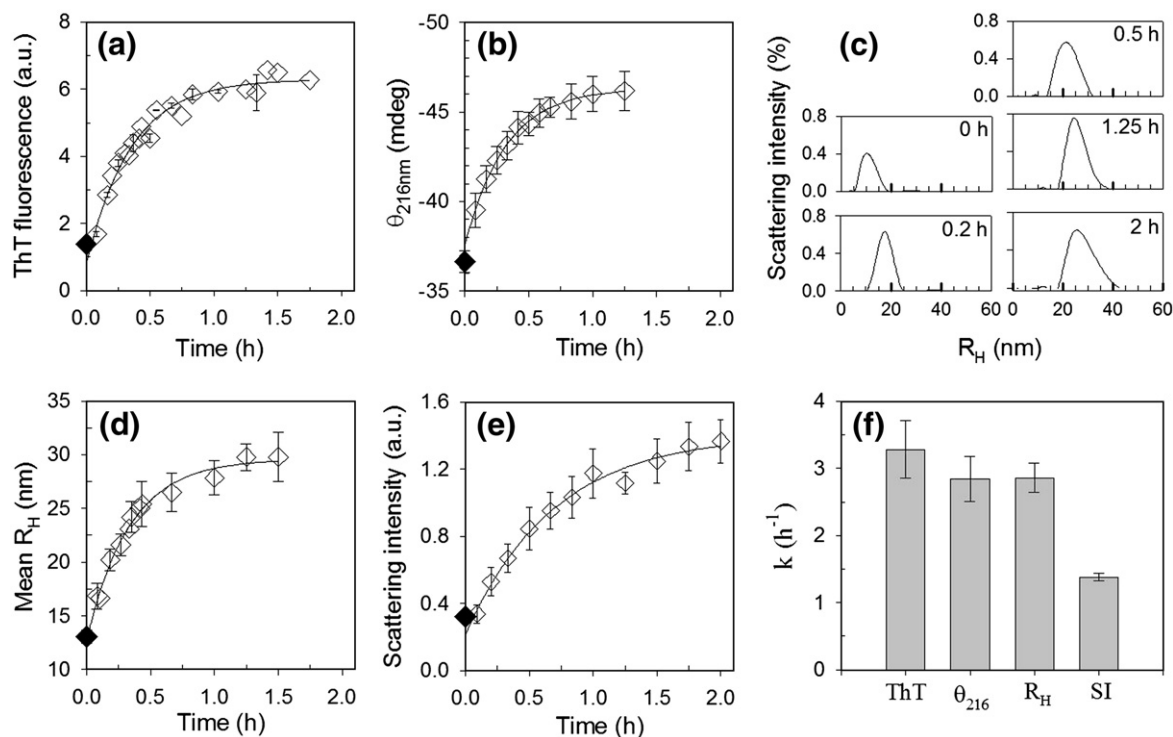


**Fig. 3.** Kinetics of formation of worm-like amyloid fibrils by 25  $\mu\text{M}$  moPrP at 60  $^{\circ}\text{C}$ , pH 2. (a) ThT-fluorescence-monitored kinetics. (b) Ellipticity at 216 nm,  $\theta_{216}$ -monitored kinetics. (c) Hydrodynamic radius distributions of aggregated protein at 0, 0.2, 0.5, 1.25, and 2 h of aggregation. (d) Mean  $R_{\text{H}}$ -monitored kinetics. (e) Total SI-monitored kinetics. The continuous lines through the data points in (a), (b), (d), and (e) are least-squares fits to a single-exponential equation. In (a), (b), (d), and (e), the filled symbol at  $t = 0$  represents the signal of the protein after 1 h incubation at pH 2, 25  $^{\circ}\text{C}$ , prior to heating to 60  $^{\circ}\text{C}$ . (f) Bar chart showing apparent rate constants measured by ThT-fluorescence-,  $\theta_{216}$ -,  $R_{\text{H}}$ -, and SI-monitored aggregation kinetics. The error bars in (a), (b), (d)–(f) represent the standard deviations calculated from three separate experiments.

tored by a change in either ThT fluorescence or  $\theta_{216}$ . Figure 3c shows the distributions of  $R_{\text{H}}$  of the  $\beta$ -rich oligomer (the species prior to heating) and those of the aggregates formed at four different time points during fibrillation at 60  $^{\circ}\text{C}$ . It is seen that the  $\beta$ -rich oligomers disappear early and are replaced by larger oligomers whose size increases progressively with time. The transformation into worm-like amyloid fibrils also leads to an increase in the heterogeneity of the population upon heating, as evident from the increase in the width of the distribution of  $R_{\text{H}}$ . From such plots of the  $R_{\text{H}}$  distribution, the mean  $R_{\text{H}}$  and SI can be determined. Figure 3d and e show the kinetics of amyloid fibrillation as monitored by an increase in the mean  $R_{\text{H}}$  and in the SI. In both cases, the kinetics are monophasic with no apparent lag phase. Each of the kinetic traces extrapolates at  $t=0$  to the signal obtained for the  $\beta$ -rich oligomer.

The apparent rate constants for the formation of worm-like amyloid fibrils, as monitored by the four different structural probes, are shown in Fig. 3f. The observed rates are similar for the ThT-fluorescence-,  $\theta_{216}$ -, and  $R_{\text{H}}$ -monitored kinetics. The SI-monitored kinetics are, however, approximately twofold slower. The experiments with each of the probes were highly reproducible, as evident from the small errors seen in each of the measurements (Fig. 3a, b, d–f).

### Temperature dependence of the formation of worm-like amyloid fibrils

Figure 4a shows the ThT fluorescence-monitored kinetics of formation of worm-like amyloid fibrils at four different temperatures: 37, 45, 50, and 60  $^{\circ}\text{C}$ . The kinetics of amyloid fibrillation at 25  $^{\circ}\text{C}$  are shown in the inset of Fig. 4b. At each of the temperatures, no lag phase is seen, and the kinetics appear monophasic. The observed rate of amyloid fibrillation increases with an increase in temperature. In Fig. 4b, the apparent rate constant is plotted against  $1/T$ . A linear Arrhenius relationship is seen. The activation energy, as determined from the Arrhenius plot, is found to be 129 kJ/mol. In Fig. 4c, it is seen that the amplitudes of the change in ThT fluorescence upon amyloid fibrillation are similar at all the temperatures.

### Protein concentration dependence of the kinetics of amyloid fibrillation

The kinetics of formation of worm-like fibrils were studied at 60  $^{\circ}\text{C}$  over a range of protein concentrations. Figure 5a and b show the protein concentration dependence of the kinetics as monitored by ThT fluorescence and  $\theta_{216}$ , respectively. The observed rate increases with an increase in protein concentration in

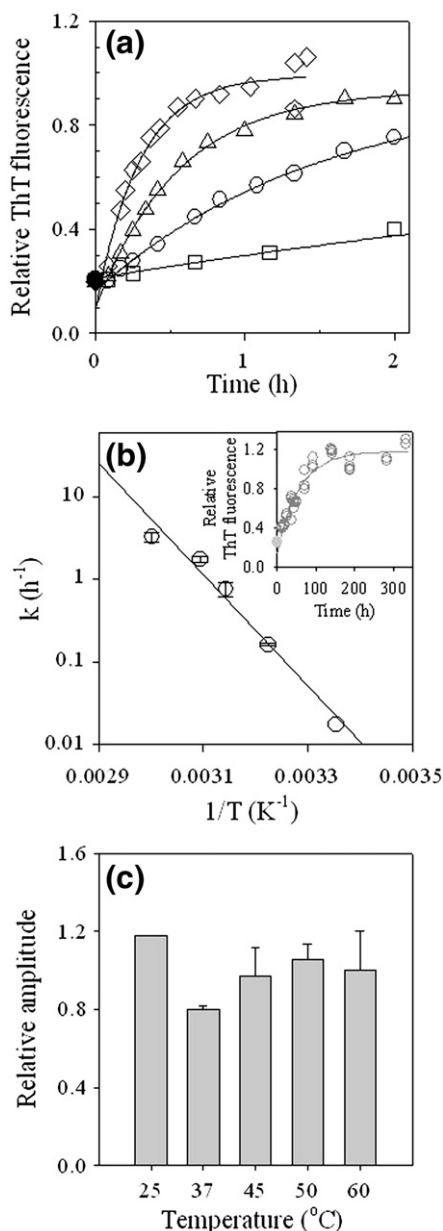


**Fig. 4.** Temperature dependence of the kinetics of amyloid fibrillation by 25  $\mu\text{M}$  moPrP at pH 2. (a) ThT-fluorescence-monitored kinetics of amyloid fibrillation at 37  $^{\circ}\text{C}$  ( $\square$ ), 45  $^{\circ}\text{C}$  ( $\circ$ ), 50  $^{\circ}\text{C}$  ( $\Delta$ ), and 60  $^{\circ}\text{C}$  ( $\diamond$ ). At each temperature, the signal is normalized relative to the final signal (at  $t = \infty$ ) at 60  $^{\circ}\text{C}$ . Representative plots are shown for each temperature. The continuous lines through the data points at each temperature are least-squares fits to a single-exponential equation. (b) Arrhenius plot: the observed rate constant is plotted against  $1/T$  ( $\text{K}^{-1}$ ). The error bars represent the standard deviations calculated from three separate experiments. A linear fit through the data points yields activation energy of 129 kJ/mol for amyloid fibrillation from the  $\beta$ -rich soluble oligomers. The inset in (b) shows the ThT-fluorescence-monitored aggregation kinetics at 25  $^{\circ}\text{C}$ . (c) Relative amplitude of the change in ThT fluorescence is plotted against temperature. At each temperature, the amplitude of the change in ThT fluorescence is normalized to the amplitude of the change in ThT fluorescence at 60  $^{\circ}\text{C}$ .

the range 10 to 50  $\mu\text{M}$ . It is seen that the kinetics are monophasic at each protein concentration.

In Fig. 5c, the apparent rate constants, obtained from the ThT-,  $\theta_{2167}$ - and  $R_{\text{H}}$ -monitored kinetics, are plotted against protein concentration. At each protein concentration, the observed rate appears to be independent of the probe used. Moreover, the concentration dependences of the observed rate constants are also similar. For all the probes, the observed rate constant appears to have an apparently sigmoidal dependence on protein concentration and reaches a limiting value at a protein concentration of  $\sim 50$   $\mu\text{M}$ . The dependence of the observed rate constant on protein concentration is, however, weak: a plot of log rate *versus* log concentration has a slope of only 1.6 (inset in Fig. 5c).

In Fig. 5d, the apparent rate constant of fibrillation is plotted against the concentration of  $\beta$ -rich oligomer. The concentration of the  $\beta$ -rich oligomer at each total (monomeric) protein concentration was determined as described in the figure legend. The apparent rate constant increases linearly with an increase in the concentration of  $\beta$ -rich oligomer. The inset in Fig. 5d shows that the apparent rate decreases linearly with an increase in the concentration of  $\alpha$ -rich monomer.

#### Dependence of fibril size on protein concentration

Figure 6a shows the distributions of  $R_{\text{H}}$  of the worm-like amyloid fibrils formed at three different protein concentrations (5, 10, and 25  $\mu\text{M}$ ). At each protein concentration, the measurement was made at a time corresponding to three time constants of the ThT-fluorescence-monitored kinetics ( $3\tau_{\text{ThT}}$ ). The worm-like amyloid fibrils formed at the lower protein concentrations not only have a longer mean  $R_{\text{H}}$ , but they are also more heterogeneous than those formed at the higher protein concentrations, as evident from an increase in the width of the distributions with a decrease in protein concentration.

Figure 6b shows the protein concentration dependence of the mean  $R_{\text{H}}$  of the worm-like amyloid fibrils formed at a time corresponding to  $3\tau_{\text{ThT}}$ . The mean  $R_{\text{H}}$  is seen to decrease with increasing protein concentration and reaches a limiting value of 29 nm at high protein concentrations. The diameter of the worm-like amyloid fibrils, as determined from fibril heights in AFM images, is the same (2 nm) at each of the protein concentrations. For a given  $R_{\text{H}}$  and a given diameter of the worm-like amyloid fibrils, it is possible to calculate their length using Eq. (1), assuming them to be straight cylinders.<sup>51,52</sup> The dependence of the calculated lengths of the worm-like amyloid fibrils on the protein concentration is shown in the inset in Fig. 6b. It is seen that the length of the worm-like amyloid fibrils is sensitive to the protein concentration used for the aggregation reaction. The mean length of the worm-like amyloid fibrils first decreases with an increase in protein concentration and then reaches a limiting value of about 320 nm at a concentration of  $\sim 25$   $\mu\text{M}$ .

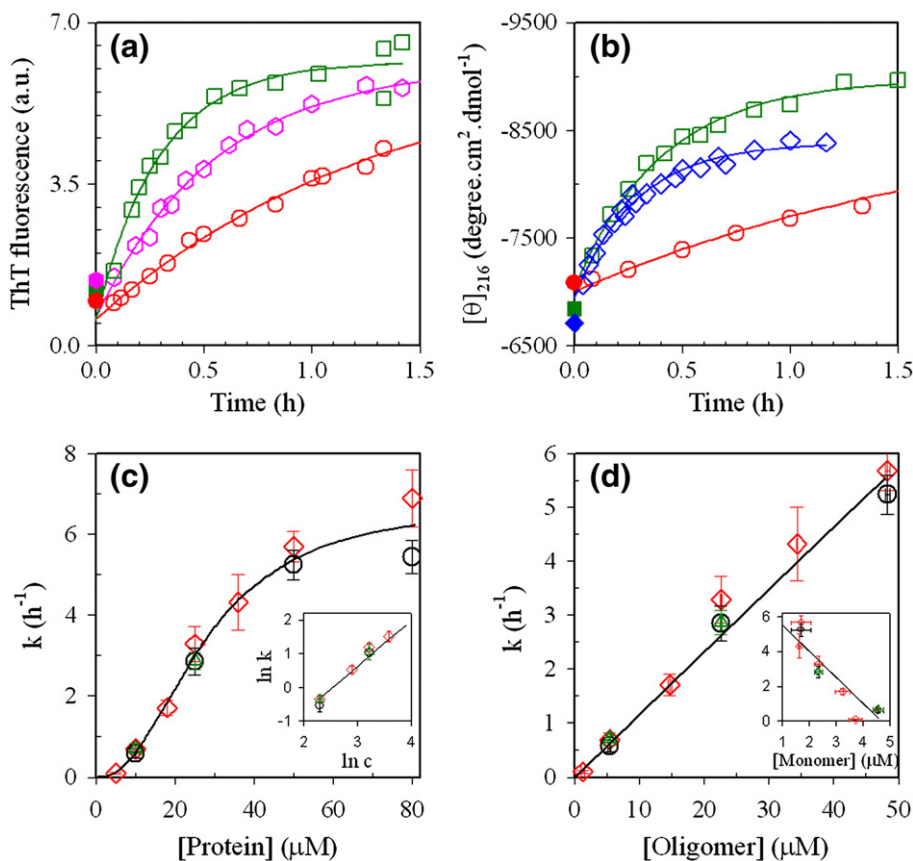


**Fig. 5.** Protein concentration dependence of the kinetics of formation of worm-like fibrils at 60 °C, pH 2. (a) ThT-fluorescence-monitored aggregation kinetics of 10  $\mu\text{M}$  (red circle), 18  $\mu\text{M}$  (pink hexagon), and 25  $\mu\text{M}$  (green square) protein. (b)  $\theta_{216}$ -monitored aggregation kinetics at 10  $\mu\text{M}$  (red circle), 25  $\mu\text{M}$  (green square), and 50  $\mu\text{M}$  (blue diamond) protein. In (a) and (b), representative plots are shown for each of the protein concentrations. The continuous lines through the data points represent the least-squares fits to a single-exponential equation. (c) The apparent rate constants of amyloid fibrillation obtained from the ThT fluorescence (red diamond),  $\theta_{216}$  (black circle), and  $R_H$  (green triangle) measured kinetics are plotted against protein concentration. The line through the data was drawn by inspection only. The inset shows the data obtained in the concentration range 10 to 36  $\mu\text{M}$ , on logarithmic axes. (d) The apparent rate constants of amyloid fibrillation obtained from the ThT fluorescence (red diamond),  $\theta_{216}$  (black circle), and  $R_H$  (green triangle) measured kinetics are plotted against the  $\beta$ -rich oligomer concentration and against the  $\alpha$ -rich monomer concentration (inset). The concentrations of the  $\beta$ -rich oligomer and the  $\alpha$ -rich monomer at each protein concentration were determined by multiplying the fractions of protein present as the  $\beta$ -rich oligomer and  $\alpha$ -rich monomer, respectively (Fig. 2), by the total monomeric protein concentration. The straight lines through the data are least-squares fits. The error bars represent the standard deviations calculated from three separate experiments.

Figure 6c shows AFM images of the worm-like amyloid fibrils formed at the three different protein concentrations (5, 10, and 25  $\mu\text{M}$ ), at a time corresponding to  $3\tau_{\text{ThT}}$  for each protein concentration. Consistent with the DLS measurements, shown in Fig. 6a and b, the AFM images show that the worm-like amyloid fibrils formed at the lower protein concentrations are longer than those formed at the higher protein concentrations. Relatively fewer worm-like fibrils appear to have formed at the lower protein concentrations, while numerous worm-like fibrils are formed at the higher protein concentrations.

## Discussion

In the present study, the aggregation of the full-length moPrP has been studied at pH 2 in the presence of salt. The  $\beta$ -rich oligomers formed at the low

pH are found to transform into worm-like amyloid fibrils in a slow process that becomes faster at higher temperatures. The kinetics of formation of worm-like fibrils from the  $\beta$ -rich oligomer have been monitored using four different structural probes in a range of temperatures and at different protein concentrations. The length of the worm-like fibrils is found to depend on the protein concentration. The steps involved in aggregation and the possible reasons for the protein concentration dependence of the length of worm-like amyloid fibrils are discussed.

### Native protein is transformed into $\beta$ -rich oligomers and $\alpha$ -rich monomers at low pH in the presence of salt

In earlier studies, when unfolded prion protein (truncated as well as full-length), was refolded by dilution of denaturant, it transformed into  $\beta$ -

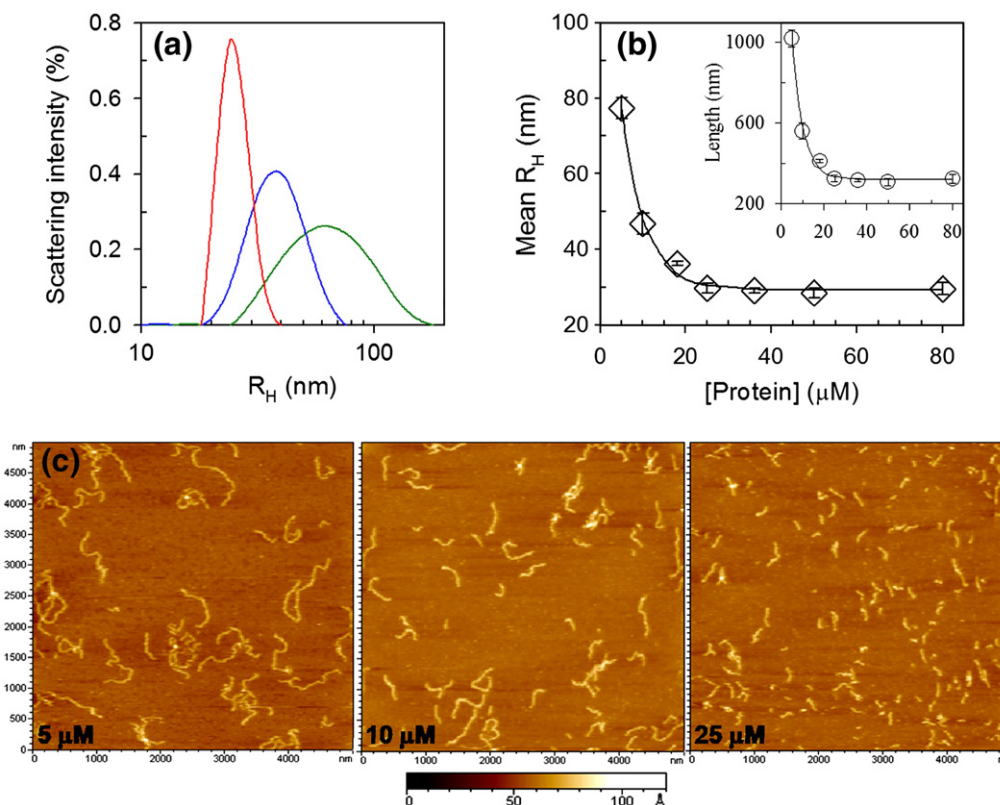


**Fig. 6.** Dependence of the size of worm-like fibrils on protein concentration at 60 °C, pH 2. (a) Distribution of hydrodynamic radii of the worm-like amyloid fibrils formed at 5  $\mu$ M (green line), 10  $\mu$ M (blue line), and 25  $\mu$ M (red line) protein concentrations. (b) Dependence of the mean  $R_H$  of the worm-like amyloid fibrils formed on protein concentration. The inset shows the dependence on protein concentration of the length of the worm-like fibrils, determined using Eq. (1). (c) AFM images of worm-like fibrils formed at 5, 10, and 25  $\mu$ M protein concentrations. All the measurements shown in (a)–(c) were done at times corresponding to  $3\tau_{\text{THT}}$  for each of the protein concentrations.

oligomers, which existed in slow equilibrium with monomeric PrP ( $\alpha$ -PrP).<sup>31–33,53</sup> Also in this study, it is seen that at pH 2, in the presence of 0.15 M NaCl, but in the absence of any denaturant, native full-length moPrP transforms into  $\beta$ -rich oligomers that are in equilibrium with  $\alpha$ -rich monomers (Figs. 1 and 2). The  $\beta$ -rich oligomer has a far-UV CD spectrum similar to that of the previously reported  $\beta$ -oligomer. The sizes of the two are, however, different. The previously reported  $\beta$ -oligomers were shown to be octamers,<sup>32</sup> while the  $\beta$ -rich oligomers observed in this study are found to be much larger, as seen in the gel-filtration chromatography elution profile (Fig. 2b). In the earlier studies,<sup>32,33</sup> the  $\beta$ -oligomer was characterized in a buffer containing 1 M guanidine hydrochloride as well as 3 M urea. It is possible that its size is smaller than the  $\beta$ -rich oligomer characterized in this study, only because of the presence of the two denaturants. The previously characterized  $\alpha$ -PrP<sup>33</sup> and the  $\alpha$ -rich monomer characterized in this study appear to have similar far-UV CD spectra, but it is likely that the former is partially unfolded because of the presence of 1 M guanidine hydrochloride and 3 M urea. At present, it is not known how much of native moPrP structure is retained in either the  $\alpha$ -PrP<sup>33</sup> or the  $\alpha$ -rich monomer.

### The $\beta$ -rich oligomer and not the $\alpha$ -rich monomer converts into worm-like amyloid fibrils

Soluble oligomers have been observed on the aggregation pathways of many proteins.<sup>54–61</sup> Their exact role in the aggregation process is, however, still controversial. At pH 2, native moPrP is converted into  $\beta$ -rich oligomers and  $\alpha$ -rich monomers, which are in slow equilibrium with each other. Either species could serve as the starting point for the formation of worm-like fibrils. The apparent rate of formation of worm-like fibrils increases linearly with an increase in  $\beta$ -rich oligomer concentration and decreases linearly with an increase in  $\alpha$ -rich monomer concentration (Fig. 5d). This result conclusively shows that the formation of worm-like amyloid fibrils proceeds directly from the  $\beta$ -rich oligomer and not from the  $\alpha$ -rich monomer. The linear dependence of the apparent rate on  $\beta$ -rich oligomer concentration also rules out the possibility that the  $\beta$ -rich oligomer disaggregates to a smaller oligomer that is the competent species to form worm-like fibrils: if it did, then the dependence of the rate on  $\beta$ -rich oligomer concentration would not be linear because the degree of dissociation into the smaller oligomer would not have a linear dependence on  $\beta$ -rich oligomer concentration. It should be

noted that the kinetic data points (Figs. 3–5) extrapolate in an apparently single-exponential manner to the signal of the  $\beta$ -rich oligomers at  $t = 0$ , at each of the temperatures (Fig. 4a and b, inset), and for each of the four probes (Fig. 3a, b, d, and e) that measure four different structural aspects of the aggregation process. This is expected when the  $\beta$ -rich oligomer acts as a direct precursor for the formation of worm-like amyloid fibrils.

In previous studies of the aggregation of full-length moPrP, the formation of long straight amyloid fibrils had been observed in conditions where the monomeric  $\alpha$ -PrP, and not the  $\beta$ -oligomer, was predominantly populated.<sup>33</sup> It was therefore suggested that  $\alpha$ -PrP transformed into the long straight amyloid fibrils and that the  $\beta$ -oligomers were off-pathway to the formation of straight amyloid fibrils.<sup>32,33</sup> In this study, it has been shown that the  $\beta$ -rich oligomers are instead on the pathway of formation of worm-like amyloid fibrils. It is likely that the transformation of  $\beta$ -oligomers into worm-like fibrils had not been observed in the earlier studies<sup>32,33</sup> because they were carried out in the presence of 1 M guanidine hydrochloride and 3 M urea, which could suppress the formation of worm-like amyloid fibrils by causing dissociation of the  $\beta$ -rich oligomer into the smaller  $\beta$ -oligomer.<sup>33,62</sup>

The transformation of  $\alpha$ -Prp into long straight fibrils is faster at higher pH where  $\alpha$ -Prp is populated preferentially over the  $\beta$ -oligomer.<sup>33</sup> Similarly, the transformation of  $\beta$ -rich oligomer into worm-like fibrils will become slower at neutral pH because the concentration of the  $\beta$ -rich oligomer will be very low. But given that the prion diseases are slow-onset diseases,<sup>2,3,25</sup> the possibility that the worm-like fibrils play a role in PrP toxicity cannot be ruled out now. Future work will address the question of whether the worm-like fibrils are toxic in the first place.

### Fibrillation from the $\beta$ -rich oligomers does not show any characteristic features of nucleation-dependent polymerization

The formation of worm-like amyloid fibrils by the prion protein could conceivably occur through a nucleation-dependent mechanism,<sup>11</sup> as does the formation of long straight amyloid fibrils by the same protein.<sup>63</sup> Fibrillation from the  $\beta$ -rich oligomers does not, however, show any characteristic feature of nucleation-dependent polymerization. The kinetics do not show a lag phase in the range of protein concentrations studied with any of the structural probes used (Figs. 3 and 5). The kinetics observed with each of the probes show monophasic increases in the measured signals. The protein concentration dependences of the amplitudes of the change in ThT fluorescence as well as in  $\theta_{216}$  indicate that the formation of worm-like amyloid fibrils does not involve a critical concentration below which aggregation does not occur (data not shown). The observed rate constant for the formation of worm-like fibrils shows a very weak dependence on the protein concentration (Fig. 5c, inset). If a nucleation

event does occur during the formation of worm-like fibrils, it could be a folding event in which a structural transition in the  $\beta$ -rich oligomer might serve as the nucleation event. Alternatively, the  $\beta$ -rich oligomer itself might act as the nucleus. Given the absence of the prominent features of a nucleation-dependent polymerization reaction, this mechanism seems unlikely for the formation of worm-like fibrils. Similar observations have been made for the formation of either worm-like amyloid fibrils or protofibrils by several other proteins, including  $\beta_2$ -microglobulin,<sup>50</sup> barstar,<sup>60</sup> transthyretin,<sup>64</sup> and amyloid- $\beta$ .<sup>65</sup>

### Transformation of $\beta$ -rich oligomers into worm-like amyloid fibrils occurs in multiple steps

The observation that the rate of formation of worm-like fibrils first increases and then saturates at higher protein concentrations suggests that the process occurs in steps and that the rate-determining steps at lower and higher protein concentrations are different (Fig. 5c). At lower protein concentrations, the apparent rate of amyloid fibrillation appears to be limited by the association of the protein molecules; hence, the observed rate increases with an increase in protein concentration. At higher protein concentrations, where the association rate has become sufficiently fast, a conformational conversion reaction appears to take over as the rate-determining step; hence, the observed rate becomes independent of protein concentration. A similar saturation in the observed rate of fibrillation at high protein concentration is also observed when the aggregation reaction is carried out at 45 °C (data not shown).

During the formation of worm-like amyloid fibrils, the distribution of hydrodynamic radii changes progressively in a continuous manner (Fig. 3c). The population corresponding to  $\beta$ -rich oligomers disappears very early during the process. This suggests that the  $\beta$ -rich oligomer grows progressively in size into higher-order oligomers, which then grow into elongated aggregates. The possibility that a rapid all-or-none protein-concentration-dependent equilibrium between the  $\beta$ -rich oligomer and a specific higher-order oligomer is followed by a rate-limiting slow conformational change can, however, be ruled out because only one species is seen at any time during aggregation, and the size of the aggregate is observed to increase in a slow progressive manner in the light-scattering experiments (Fig. 3). If the  $\beta$ -rich oligomer and a specific higher-order oligomer were the only two species populated during the time course of aggregation, then two size distributions arising from these two species would have been observed at different times of aggregation, because exchange between the two species cannot be faster than the time scale of light scattering.

The  $R_H$ -monitored kinetics yield an observed rate constant similar to that obtained from the ThT-fluorescence- and  $\theta_{216}$ -monitored kinetics (Fig. 3f). This suggests that conformational conversion, which leads to the creation of ThT-binding sites and the increase in  $\beta$ -sheet content, occurs concurrently

with the elongation of aggregates. The SI-monitored kinetics are, however, slower than the kinetics monitored by  $R_H$  (Fig. 3f). SI is indicative of both the amount and the mass of aggregated particles. In AFM images, the relative amount of worm-like fibrils and spherical oligomers (seen in the AFM images) appears not to change from 1 h to 3 h (data not shown). This indicates that the increase in SI, which is not accompanied by an increase in the apparent  $R_H$ , occurs because of lateral association of the elongated aggregates,<sup>51,60</sup> which then appears to be the last step in the formation of the worm-like fibrils.

If all the steps (conformational conversion, elongation, lateral association) are sequential, then an initial lag phase should have been observed in the SI-monitored kinetics, which are the slowest. But the kinetics monitored by SI do not show any initial lag phase. One possible explanation for this observation is that the formation of the worm-like amyloid fibrils from the  $\beta$ -rich oligomers occurs by multiple routes. This issue is being addressed in ongoing work.

### Conformational conversion occurs during the formation of worm-like amyloid fibrils from the $\beta$ -rich oligomers

The activation-energy barrier obtained for the formation of worm-like amyloid fibrils by moPrP is 129 kJ/mol. Similar values have been obtained for the aggregation of many other proteins, such as barstar,<sup>60</sup> amyloid- $\beta$  protein,<sup>66</sup>  $\alpha$ -synuclein,<sup>67</sup> and human insulin,<sup>68</sup> and it is likely that the large activation energy arises because of the complexity of the protein association reactions that define the aggregation process. On the other hand, the observed activation-energy barrier is very similar in magnitude to that seen for proline isomerization reactions. Thus, the conformational conversion step, which becomes the rate-limiting step at higher protein concentrations, and which leads to an increase in  $\beta$ -sheet structure, might be accompanied by a proline isomerization reaction. Although the proline isomerization reaction is much faster than the observed rate of aggregation, this hypothesis may be valid under conditions where the proline isomerization reactions in each oligomer are triggered only upon addition of the oligomer to the elongating fibril, along with the conformational conversion within the fibril. Proline isomerization is seen as the rate-limiting step in the formation of the stefin B tetramer<sup>69</sup> and in the formation of an amyloidogenic intermediate in the folding reaction of  $\beta_2$ -microglobulin.<sup>70</sup> It is well known that the proline isomerization reaction constitutes the rate-determining step in the folding reactions of many proteins. It may be that the process of protein aggregation is also limited by a proline isomerization reaction.<sup>60</sup>

### The length of the worm-like amyloid fibrils depends on the protein concentration

At lower protein concentrations, where the rate of growth of worm-like fibrils is slower, longer fibrils

are formed (Fig. 6). At higher protein concentrations, where fibril growth is faster, smaller fibrils are formed. The length of protein aggregates has been shown to depend on protein concentration for many proteins, including amyloid- $\beta$ <sup>71</sup> and  $\beta_2$ -microglobulin.<sup>72</sup> The greater heterogeneity seen in the length of the worm-like fibrils formed at lower protein concentrations (Fig. 6a) might be a consequence of their longer length, which could make them more susceptible to breakage.

The observation that longer worm-like fibrils are formed at lower protein concentrations suggests that the  $\beta$ -rich oligomers do not directly transform into the worm-like fibrils. It appears that the  $\beta$ -rich oligomers assemble to form critical higher-order oligomers of a defined size, which are competent to form the worm-like amyloid fibrils. The concentration of such critical higher-order oligomers will depend on the protein concentration. At higher protein concentrations, there will be a larger number of the critical oligomers formed as aggregation proceeds, and hence, more sites from which fibrillation can commence. At lower protein concentrations, there will be a smaller number of critical oligomers formed under the aggregation conditions, and hence, fewer sites from which fibrillation can commence. If growth into the worm-like fibrils occurs by the addition of smaller aggregates to the critical oligomers, then there will be longer but fewer fibrils formed at a lower protein concentration because there are fewer critical oligomers and a larger proportion of smaller aggregates that can add to the critical oligomers to form the worm-like fibrils. Conversely, there will be shorter but more fibrils formed at a higher protein concentration because there are more critical oligomers, and correspondingly fewer small aggregates that can add to the critical oligomers to form the worm-like fibrils. A similar mechanism appears to describe the aggregation of amyloid- $\beta$  protein, for which it was suggested that the critical oligomers are micellar structures that grow into protofibrils by addition of monomeric protein.<sup>71</sup>

### Mechanism of formation of worm-like amyloid fibrils by the full-length mouse prion protein

Figure 7 depicts the process of amyloid fibrillation by moPrP. The  $\beta$ -rich oligomers initially grow continuously to form critical higher-order oligomers, which remain in equilibrium with the smaller oligomers. The critical higher-order oligomers are the species that are competent to elongate into worm-like fibrils. Conformational changes that lead to an increase in  $\beta$ -sheet content and to the creation of ThT binding sites occur concomitantly with the elongation reaction. It is, however, not known at present whether the conformational change is driven by the elongation process, as has been suggested in the case of the yeast prion protein, Sup35,<sup>55,73</sup> and amyloid- $\beta$ ,<sup>74</sup> or whether the conformational change immediately precedes, and is a prerequisite to, elongation. Finally, it appears that the elongated aggregates associate laterally to form mature worm-like fibrils.

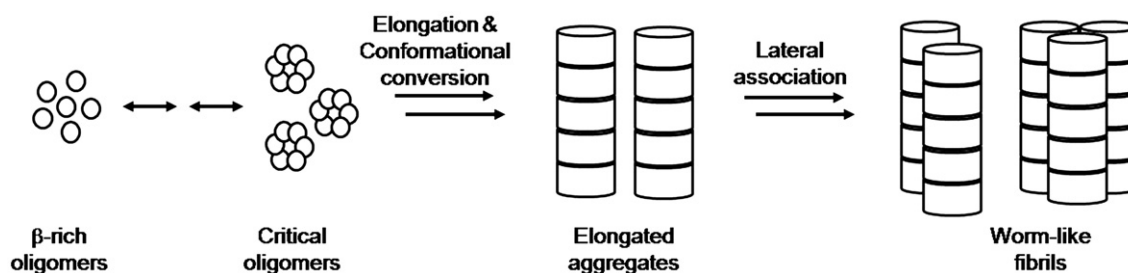


**Fig. 7.** Model for the formation of worm-like amyloid fibrils by the moPrP. The  $\beta$ -rich oligomers equilibrate with large oligomers, including elongation-competent critical oligomers. The critical oligomer grows by addition of smaller oligomers. Elongation occurs simultaneously with conformational change during fibrillation. Finally, the elongated aggregates appear to associate laterally to form mature worm-like fibrils.

Finally, the results presented here and elsewhere<sup>33</sup> indicate that there are two pathways for the formation of amyloid fibrils by the moPrP. One pathway starting from the  $\alpha$ -monomer leads to the formation of long straight amyloid fibrils in a process that appears to be nucleation dependent.<sup>33,63</sup> The other pathway, delineated in this study, starts from the  $\beta$ -rich oligomer and leads to the formation of worm-like amyloid fibrils. In this respect, the fibrillation of moPrP at low pH is remarkably similar to that of  $\beta^2$ -microglobulin.<sup>50</sup> In both cases, a monomer leads to nucleation-dependent formation of long straight fibrils, while an oligomer leads to the formation of worm-like fibrils in a process that does not appear to be nucleation dependent. In both cases, it appears that the two pathways are operative under different environmental conditions.<sup>33,50</sup> It remains to be seen whether these features of fibril formation are also shared by other aggregating proteins.

## Materials and Methods

### Protein expression and purification

*Escherichia coli* BL21 (DE3) codon plus (Stratagene) cells were transformed with a pET17b plasmid<sup>62</sup> containing the full-length sequence (23–231) of the moPrP gene. The cells were grown at 37 °C in rich medium containing 100  $\mu$ g/mL ampicillin, and the protein (moPrP23–231) was found to be expressed in inclusion bodies. Inclusion bodies were dissolved in a buffer containing 6 M guanidinium hydrochloride, and purification and refolding were carried out on a Ni<sup>2+</sup> Sepharose column (Amersham). The protein was further purified by reverse-phase chromatography using a Resource RPC column. The purity of the protein was confirmed by SDS-PAGE and electrospray ionization–mass spectrometry. The mass of the protein was the expected 23,236 Da when determined by mass spectrometry using an ESI–quadrupole time-of-flight mass spectrometer from Waters. Typically, 40 to 50 mg of the protein was obtained from 1 l of *E. coli* culture. The protein was transferred to 10 mM sodium acetate buffer (pH 4) by using an Amicon ultrafiltration cell and stored at –80 °C. The protein concentration was determined from the absorbance at 280 nm, using an extinction coefficient of 62,160 M<sup>–1</sup> cm<sup>–1</sup>.<sup>62</sup>

### Buffers, solutions, and experimental conditions

All reagents used for experiments were of the highest-purity grade available from Sigma. The protein in 10 mM sodium acetate buffer (pH 4) was diluted twofold with 2 $\times$  aggregation buffer (100 mM glycine, 0.3 M NaCl, pH 2), so that the protein was finally in 50 mM glycine, 0.15 M NaCl, pH 2. The final protein concentration used for most of the experiments was 25  $\mu$ M except for the concentration-dependence studies, where it was varied between 5 and 80  $\mu$ M.

### Aggregation studies

The aggregation process was monitored by measurement of ThT fluorescence, of ellipticity at 216 nm ( $\theta_{216}$ ), and of DLS. For all the measurements, the protein was first incubated for 1 h in 50 mM glycine, 0.15 M NaCl, pH 2, at 25 °C, prior to the temperature jump. After incubation for 1 h, the protein was transferred into a tube on the heating block preset at the desired final temperature (37 $\pm$ 0.5 to 60 $\pm$ 0.5 °C). The same heating block was used for all the experiments to reduce variability. The desired temperature was reached within 4 min of incubation of the protein in the heating block. At different time points of aggregation, aliquots of the protein sample were withdrawn for analysis by ThT fluorescence,  $\theta_{216}$ , and DLS. All the sample aliquots withdrawn for analysis by the different probes were treated in as similar a manner as possible.

It was important to show that prolonged incubation of the protein at pH 2, 60 °C, did not result in hydrolysis of the polypeptide chain. A sample of protein that had been incubated for 10 h at pH 2, 60 °C, was therefore subject to SDS-PAGE. No significant hydrolysis of the protein was observed (data not shown).

### ThT fluorescence assay

The ThT assay was done at pH 8 in 50 mM Tris–HCl buffer. For the assay, a final concentration of 2  $\mu$ M of protein and 20  $\mu$ M of ThT was used. A calculated amount of the protein (according to the concentration used in the aggregation experiment) was withdrawn from the sample and added to the ThT assay solution. ThT fluorescence was measured using a Fluoromax-3 spectrofluorimeter (Jobin Yvon). The experimental settings used were as follows: excitation wavelength, 440 nm; emission wavelength, 482 nm; excitation bandwidth, 1 nm; and emission bandwidth, 10 nm. Measurements were made within half a minute of the addition of the protein to the assay

solution. The emission spectra of 20  $\mu\text{M}$  ThT alone and that with 2  $\mu\text{M}$  protein were collected with the excitation wavelength set at 440 nm. The excitation and emission bandwidths were 1 and 10 nm, respectively.

### Circular dichroism measurements

A Jasco J-720 spectropolarimeter was used for the far UV CD measurements. Cuvettes of 0.5-, 1-, and 2-mm path length were used for the measurements. Spectra were collected in the wavelength range 200 to 250 nm. The instrument settings used were as follows: step resolution, 1 nm; scan speed, 100 nm/min; and bandwidth, 1 nm. Each spectrum was averaged for over 30 scans. For the kinetic studies,  $\theta_{216}$ , the ellipticity at 216 nm, was monitored. An aliquot of the protein sample was withdrawn from the sample and  $\theta_{216}$  was measured at regular time intervals. In the case of the aggregation of 80  $\mu\text{M}$  protein, the protein was diluted to 25  $\mu\text{M}$  just before the measurement.

### Dynamic light-scattering measurements

A DynaPro-99 unit (Protein Solutions Ltd) was used for the DLS measurements. To remove dust particles, all the buffers and the protein solution at pH 4 were filtered using 0.02- $\mu\text{m}$  filters. Filtered buffers and the protein solution at pH 4 were spun at 10,000 rpm for 10 min. The tubes and tips used for the experiment were washed three times with 0.02- $\mu\text{m}$ -filtered water before use. The pH jump from 4 to 2 was given with the 0.02- $\mu\text{m}$ -filtered buffer. The protein sample was incubated for 1 h at room temperature before the temperature jump. After the temperature jump, aliquots of the protein sample were withdrawn for the measurement at regular time intervals. The protein sample was cooled to 25  $^{\circ}\text{C}$  and then placed in a 45- $\mu\text{l}$  cuvette. The cuvette was placed in the sample chamber maintained at 25  $^{\circ}\text{C}$ . The experimental settings used were as follows: acquisition time, 5 s; S/N threshold, 2.5; and sensitivity, 80%. The sample was illuminated with a laser of wavelength 829.4 nm, and the scattering intensity at 90 $^{\circ}$  and its autocorrelation function were measured simultaneously. Fluctuations more than 15% in the scattering intensity were excluded from analysis. The DynaLS software (Protein Solutions Ltd) was used to resolve the accepted acquisitions into well-defined Gaussian distributions of hydrodynamic radii. The viscosities of the solutions were determined from refractive index measurements. The total light-scattering intensity (counts per second) was determined from cumulant analysis as the mean of all accepted acquisitions.

The length ( $L$ ) of the worm-like fibrils was calculated using the following equation:<sup>52</sup>

$$R_H = \frac{L}{2} \left( \frac{\sqrt{1-x^2}}{\ln \frac{1+\sqrt{1-x^2}}{x}} \right) \quad (1)$$

where

$$x = \frac{d}{L} \left[ 1 + \frac{0.37(L-d)}{L} \right]$$

The mean hydrodynamic radius ( $R_H$ ) and diameter ( $d$ ) of the worm-like fibrils were determined from DLS measurements and AFM images, respectively.

### Size-exclusion chromatography

The hydrodynamic properties of moPrP were studied using gel filtration on a Waters Protein Pak 300-SW column using an Akta (GE) chromatography system. The fractionation range of the 15.1-mL column was 10 to 300 kDa, and the void volume was determined to be 6.2 mL. Each protein sample was equilibrated in 50 mM glycine, 0.15 M NaCl, pH 2, for 1 h prior to the chromatography run. The column was equilibrated with the same buffer by passing four column volumes of the buffer through it before injecting 50  $\mu\text{l}$  of the protein solution. A flow rate of 0.72 mL/min was used.

### Atomic force microscopy

For the AFM study, protein in 50 mM glycine, 0.15 M NaCl buffer at pH 2 was heated to 60  $^{\circ}\text{C}$ . An aliquot of the sample was withdrawn and diluted to 0.5  $\mu\text{M}$  in the pH 2 aggregation buffer. It was applied on freshly cleaved mica and allowed to incubate for 1 min. The mica surface was then rinsed three times with filtered water at pH 2 and dried under vacuum for 45 min before it was scanned. The AFM images were obtained on a PicoPlus AFM instrument (Molecular Imaging Inc., Arizona) operating in the noncontact mode.

### Acknowledgements

We thank Marc Jamin for providing us with the plasmid containing the gene for the full-length mouse prion protein used in this study. We thank members of our laboratory for discussions, and for comments on the manuscript. The AFM images were collected in the Central Imaging Facility of NCBS. This work was funded by the Tata Institute of Fundamental Research. JBU is a recipient of a JC Bose National Research Fellowship from the Government of India.

### References

1. Prusiner, S. B. (1998). Prions. *Proc. Natl Acad. Sci. USA*, **95**, 13363–13383.
2. Horiuchi, M. & Caughey, B. (1999). Prion protein interconversions and the transmissible spongiform encephalopathies. *Structure*, **7**, R231–R240.
3. Collinge, J. (2001). Prion diseases of humans and animals: their causes and molecular basis. *Annu. Rev. Neurosci.* **24**, 519–550.
4. Aguzzi, A. & Polymenidou, M. (2004). Mammalian prion biology: one century of evolving concepts. *Cell*, **116**, 313–327.
5. Chien, P., Weissman, J. S. & DePace, A. H. (2004). Emerging principles of conformation-based prion inheritance. *Annu. Rev. Biochem.* **73**, 617–656.
6. Weissmann, C. (2004). The state of the prion. *Nat. Rev. Microbiol.* **11**, 861–871.
7. Caughey, B. & Baron, G. S. (2006). Prions and their partners in crime. *Nature*, **443**, 803–810.
8. Prusiner, S. B. (1982). Novel proteinaceous infectious particles cause scrapie. *Science*, **216**, 136–144.
9. Cohen, F. E., Pan, K. M., Huang, Z., Baldwin, M.,

- Fletterick, R. J. & Prusiner, S. B. (1994). Structural clues of prion replication. *Science*, **264**, 530–531.
10. Griffith, J. S. (1967). Self-replication and scrapie. *Nature*, **215**, 1043–1044.
  11. Harper, J. D. & Lansbury, P. T. (1997). Models of amyloid seeding in Alzheimer's disease and scrapie: mechanistic truths and physiological consequences of the time dependent solubility of amyloid proteins. *Annu. Rev. Biochem.* **66**, 385–407.
  12. Diring, H., Gelderblom, H., Hilmert, H., Ozel, M., Edelbluth, C. & Kimberlin, R. H. (1983). Scrapie infectivity, fibrils and low molecular weight protein. *Nature*, **306**, 476–478.
  13. Merz, P. A., Kascak, R. J., Rubenstein, R., Carp, R. I. & Wisniewski, H. M. (1987). Antisera to scrapie associated fibril protein and prion protein decorate scrapie associated fibril. *J. Virol.* **61**, 42–49.
  14. Diener, T. O. (1987). PrP and the nature of the scrapie agent. *Cell*, **49**, 719–721.
  15. Chesebro, B. (1997). Human TSE diseases—viral or protein only? *Nat. Med.* **3**, 491–492.
  16. Caughey, B. & Chesebro, B. (1997). Prion protein and the transmissible spongiform encephalopathies. *Tr. Cell. Biol.* **7**, 56–62.
  17. Swietnicki, W., Morillas, M., Chen, S. G., Gambetti, P. & Surewicz, W. K. (2000). Aggregation and fibrillization of the recombinant human prion protein huPrP90–231. *Biochemistry*, **39**, 424–431.
  18. Legname, G., Baskakov, I. V., Nguyen, H. O. B., Riesner, D., Cohen, F. E., DeArmond, S. J. & Prusiner, S. B. (2004). Synthetic mammalian prion. *Science*, **305**, 673–676.
  19. Jackson, G. S. & Clarke, A. R. (2000). Mammalian prion proteins. *Curr. Opin. Struct. Biol.* **10**, 69–74.
  20. Anderson, M., Bocharova, O. V., Makarava, N., Breydo, L., Salnikov, V. V. & Baskakov, I. V. (2006). Polymorphism and ultrastructural organization of prion protein amyloid fibrils: an insight from high resolution atomic force microscopy. *J. Mol. Biol.* **358**, 580–596.
  21. Bessen, R. A. & Marsh, R. F. (1992). Biochemical and physical properties of the prion protein from two strains of the transmissible mink encephalopathy agent. *J. Virol.* **66**, 2096–2101.
  22. Bessen, R. A. & Marsh, R. F. (1994). Distinct PrP properties suggest the molecular basis of strain variation in transmissible mink encephalopathy. *J. Virol.* **68**, 7859–7868.
  23. Parchi, P., Castellani, R., Capellari, S., Ghetti, B., Young, K., Chen, S. G. *et al.* (1996). Molecular basis of phenotypic variability in sporadic Creutzfeldt–Jakob disease. *Ann. Neurol.* **39**, 767–778.
  24. Collinge, J. & Rossor, M. (1996). A new variant of prion disease. *Lancet*, **347**, 916–917.
  25. Caughey, B. & Lansbury, P. T. (2003). Protofibrils, pores, fibrils, and neurodegeneration: separating the responsible protein aggregates from the innocent bystanders. *Annu. Rev. Neurosci.* **26**, 267–298.
  26. Kaye, R., Sokolov, Y., Edmonds, B., McIntire, T. M., Milton, S. C., Hall, J. E. & Glabe, C. G. (2004). Permeabilization of lipid bilayers is a common conformation-dependent activity of soluble amyloid oligomers in protein misfolding diseases. *J. Biol. Chem.* **279**, 46363–46366.
  27. Chiti, F. & Dobson, C. M. (2006). Protein misfolding, functional amyloid, and human disease. *Annu. Rev. Biochem.* **75**, 333–366.
  28. Kaye, R., Head, E., Thompson, J. L., McIntire, T. M., Milton, S. C., Cotman, C. W. & Glabe, C. G. (2003). Common structure of soluble amyloid oligomers implies common mechanism of pathogenesis. *Science*, **300**, 486–489.
  29. Eghiaian, F. (2005). Structuring the puzzle of prion propagation. *Curr. Opin. Struct. Biol.* **15**, 724–730.
  30. Silveira, J. R., Raymond, G. J., Hughson, A. G., Race, R. E., Sim, V. L., Hayes, S. F. & Caughey, B. (2005). The most infectious prion protein particles. *Nature*, **437**, 257–261.
  31. Hornemann, S. & Glockshuber, R. (1998). A scrapie-like unfolding intermediate of the prion protein domain PrP(121–231) induced by acidic pH. *Proc. Natl Acad. Sci. USA*, **95**, 6010–6014.
  32. Baskakov, I. V., Legname, G., Baldwin, M. A., Prusiner, S. B. & Cohen, F. E. (2002). Pathway complexity of prion protein assembly into amyloid. *J. Biol. Chem.* **277**, 21140–21148.
  33. Bocharova, O. V., Breydo, L., Parfenov, A. S., Salnikov, V. V. & Baskakov, I. V. (2005). *In vitro* conversion of full-length mammalian prion protein produces amyloid form with physical properties of PrPSc. *J. Mol. Biol.* **346**, 645–659.
  34. Baskakov, I. V. (2004). Autocatalytic conversion of recombinant prion proteins displays a species barrier. *J. Biol. Chem.* **279**, 7671–7677.
  35. Swietnicki, W., Petersen, R., Gambetti, P. & Surewicz, W. K. (1997). pH-dependent stability and conformation of the recombinant human prion protein PrP(90–231). *J. Biol. Chem.* **272**, 27517–27520.
  36. Zhang, H., Stockel, J., Mehlhorn, I., Groth, D., Baldwin, M. A., Prusiner, S. B. *et al.* (1997). Physical studies of conformational plasticity in a recombinant prion protein. *Biochemistry*, **36**, 3543–3553.
  37. Hosszu, L. L. P., Baxter, N. J., Jackson, G. S., Power, A., Clarke, A. R., Waltho, J. P. *et al.* (1999). Structural mobility of the human prion protein probed by backbone hydrogen exchange. *Nat. Struct. Biol.* **6**, 740–743.
  38. Baskakov, I. V., Aagaard, C., Mehlhorn, I., Wille, H., Groth, D., Baldwin, M. A. *et al.* (2000). Self-assembly of recombinant prion protein of 106 residues. *Biochemistry*, **39**, 2792–2804.
  39. Morillas, M., Vanik, D. L. & Surewicz, W. K. (2001). On the mechanism of  $\alpha$ -helix to  $\beta$ -sheet transition in the recombinant prion protein. *Biochemistry*, **40**, 6982–6987.
  40. Tattum, M. H., Cohen-Krausz, S., Khalili-Shirazi, A., Jackson, G. S., Orlova, E. V., Collinge, J. *et al.* (2006). Elongated oligomers assemble into mammalian PrP amyloid fibrils. *J. Mol. Biol.* **357**, 975–985.
  41. Liu, H., Farr-Jones, S., Ulyanov, N. B., Llinas, M., Marqusee, S., Groth, D. *et al.* (1999). Solution structure of syrian hamster prion protein rPrP(90–231). *Biochemistry*, **38**, 5362–5377.
  42. Zahn, R., Liu, A., Luhrs, T., Riek, R., Schroetter, C. V., Garcia, F. L. *et al.* (2000). NMR solution structure of the human prion protein. *Proc. Natl Acad. Sci. USA*, **97**, 145–150.
  43. Riek, R., Hornemann, S., Wider, G., Billeter, M., Glockshuber, R. & Wüthrich, K. (1996). NMR structure of the mouse prion protein domain PrP(121–231). *Nature*, **382**, 180–182.
  44. Donne, D. G., Viles, J. H., Groth, D., Mehlhorn, I., James, T. L., Cohen, F. E. *et al.* (1997). Structure of the recombinant full-length hamster prion protein PrP(29–231): the N terminus is highly flexible. *Proc. Natl Acad. Sci. USA*, **94**, 13452–13457.
  45. Cordeiro, Y., Kraineva, J., Gomes, M. P. B., Lopes, M. H., Martins, V. R., Lima, L. M. T. R. *et al.* (2005). The amino-terminal PrP domain is crucial to modulate prion misfolding and aggregation. *Biophys. J.* **89**, 2667–2676.

46. Frankenfield, K. N., Powers, E. T. & Kelly, J. W. (2005). Influence of the N-terminal domain on the aggregation properties of the prion protein. *Protein Sci.* **14**, 2154–2166.
47. Tank, E. M. H., Harris, D. A., Desai, A. A. & True, H. L. (2007). Prion protein repeat expansion results in increased aggregation and reveals phenotypic variability. *Mol. Cell. Biol.* **27**, 5445–5455.
48. Harper, J. D., Wong, S. S., Lieber, C. M. & Lansbury, P. T. (1999). Assembly of A $\beta$  amyloid protofibrils: an *in vitro* model for a possible early event in Alzheimer's disease. *Biochemistry*, **38**, 8972–8980.
49. Walsh, D. M., Hartley, D. M., Kusumoto, Y., Fezoui, Y., Condron, M. M., Lomakin, A. *et al.* (1999). Amyloid  $\beta$ -protein fibrillogenesis: structure and biological activity of protofibrillar intermediates. *J. Biol. Chem.* **274**, 25945–25952.
50. Gosal, W. S., Morten, I. J., Hewitt, E. W., Smith, D. A., Thomson, N. H. & Radford, S. E. (2005). Competing pathways determine fibril morphology in the self-assembly of  $\beta_2$ -microglobulin into amyloid. *J. Mol. Biol.* **351**, 850–864.
51. Lomakin, A., Benedek, G. B. & Teplow, D. B. (1999). Monitoring protein assembly using quasielastic light scattering microscopy. *Methods Enzymol.* **309**, 429–459.
52. de la Torre, J. G. & Bloomfield, V. A. (1981). Hydrodynamic properties of complex rigid biological macromolecules. Theory and application. *Q. Rev. Biophys.* **14**, 81–139.
53. Baskakov, I. V., Legname, G., Prusiner, S. B. & Cohen, F. E. (2001). Folding of prion protein to its native  $\alpha$ -helical conformation is under kinetic control. *J. Biol. Chem.* **276**, 19687–19690.
54. Speed, M. A., Wang, D. I. C. & King, J. (1995). Multimeric intermediates in the pathway to the aggregated inclusion body state for P22 tailspike polypeptide chains. *Protein Sci.* **4**, 900–908.
55. Serio, T. R., Cashikar, A. G., Kowal, A. S., Sawicki, G. J., Moslehi, J. J., Serpell, L. *et al.* (2000). Nucleated conformational conversion and the replication of conformational information by a prion determinant. *Science*, **289**, 1317–1321.
56. Bitan, G., Kirkitadze, M. D., Lomakin, A., Vollers, S. S., Benedek, G. B. & Teplow, D. B. (2003). Amyloid  $\beta$ -protein (A $\beta$ ) assembly: A $\beta$ 40 and A $\beta$ 42 oligomerize through distinct pathways. *Proc. Natl Acad. Sci. USA*, **100**, 330–335.
57. Modler, A. J., Gast, K., Lutsch, G. & Damaschun, G. (2003). Assembly of amyloid protofibrils via critical oligomers—a novel pathway of amyloid formation. *J. Mol. Biol.* **325**, 135–148.
58. Kaylor, J., Bodner, N., Edridge, S., Yamin, G., Hong, D. P. & Fink, A. L. (2005). Characterization of oligomeric intermediates in  $\alpha$ -synuclein fibrillation: FRET studies of Y125W/Y133F/Y136F  $\alpha$ -synuclein. *J. Mol. Biol.* **353**, 357–372.
59. Mukhopadhyay, S., Nayak, P. K., Udgaonkar, J. B. & Krishnamoorthy, G. (2006). Characterization of the formation of amyloid protofibrils from barstar by mapping residue-specific fluorescence dynamics. *J. Mol. Biol.* **358**, 935–942.
60. Kumar, S., Mohanty, S. K. & Udgaonkar, J. B. (2007). Mechanism of formation of amyloid protofibrils of barstar from soluble oligomers: evidence for multiple steps and lateral association coupled to conformational conversion. *J. Mol. Biol.* **367**, 1186–1204.
61. Chimon, S., Shaibat, M. A., Jones, C. R., Calero, D. C., Aizezi, B. & Ishii, Y. (2007). Evidence of fibril-like  $\beta$ -sheet structures in a neurotoxic amyloid intermediate of Alzheimer's  $\beta$ -amyloid. *Nat. Struct. Mol. Biol.* **14**, 1157–1164.
62. Vendrely, C., Valadie, H., Bednarova, L., Cardin, L., Padeloup, M., Cappadoro, J. *et al.* (2005). Assembly of the full-length recombinant mouse prion protein I. Formation of soluble oligomers. *Biochim. Biophys. Acta*, **1724**, 355–366.
63. Baskakov, I. V. & Bocharova, O. V. (2005). *In vitro* conversion of mammalian prion protein into amyloid fibrils displays unusual features. *Biochemistry*, **44**, 2339–2348.
64. Hurshman, A. R., White, J. T., Powers, E. T. & Kelly, J. W. (2004). Transthyretin aggregation under partially denaturing conditions is a downhill polymerization. *Biochemistry*, **43**, 7365–7381.
65. Carrotta, R., Manno, M., Bulone, D., Martorana, V. & Biagio, P. L. S. (2005). Fibrillation of amyloid  $\beta$ -protein at low pH via a non-cooperative elongation mechanism. *J. Biol. Chem.* **280**, 30001–30008.
66. Kusumoto, Y., Lomakin, A., Teplow, D. B. & Benedek, G. B. (1998). Temperature dependence of amyloid  $\beta$ -protein fibrillization. *Proc. Natl Acad. Sci. USA*, **95**, 12277–12282.
67. Uversky, V. N., Li, J. & Fink, A. L. (2001). Evidence for a partially folded intermediate in  $\alpha$ -synuclein fibril formation. *J. Biol. Chem.* **276**, 10737–10744.
68. Mauro, M., Craparo, E. F., Podesta, A., Bulone, D., Carrotta, R., Martorana, V. *et al.* (2007). Kinetics of different processes in human insulin amyloid formation. *J. Mol. Biol.* **366**, 258–274.
69. Kokalj, S. J., Gunčar, G., Štern, I., Morgan, G., Rabzelj, S., Kenig, M. *et al.* (2007). Essential role of proline isomerization in stefin B tetramer formation. *J. Mol. Biol.* **366**, 1569–1579.
70. Jahn, T. R., Parker, M. J., Homans, S. W. & Radford, S. E. (2006). Amyloid formation under physiological conditions proceeds via a native-like folding intermediate. *Nat. Struct. Mol. Biol.* **13**, 195–201.
71. Lomakin, A., Chung, D. S., Benedek, G. B., Kirschner, D. A. & Teplow, D. B. (1996). On the nucleation and growth of amyloid  $\beta$ -protein fibrils: detection of nuclei and quantitation of rate constants. *Proc. Natl Acad. Sci. USA*, **93**, 1125–1129.
72. Smith, D. P. & Radford, S. E. (2001). Role of the single disulphide bond of  $\beta^2$ -microglobulin in amyloidosis *in vitro*. *Protein Sci.* **10**, 1775–1784.
73. Scheibel, T., Bloom, J. & Lindquist, S. L. (2004). The elongation of yeast prion fibers involves separable steps of association and conversion. *Proc. Natl Acad. Sci. USA*, **101**, 2287–2292.
74. Esler, W. P., Stimson, E. R., Jennings, J. M., Vinters, H. V., Ghilardi, J. R., Lee, J. P. *et al.* (2000). Alzheimer's disease amyloid propagation by a template-dependent dock-lock mechanism. *Biochemistry*, **39**, 6288–6295.